Simulation of machining of ductile polycrystalline aggregates using a remeshing framework

A. S. Vandana, Narayan K. Sundaram*

Department of Civil Engineering, Indian Institute of Science, Bangalore, India 560012

Abstract

Simulating the cutting of soft, ductile polycrystalline aggregates like CP aluminum and annealed OFHC copper beyond the incipient stage is challenging because of the occurrence of extremely sinuous plastic flow, and the need to model microstructure, high interfacial friction, and transgranular failure. Here we present a general adaptive remeshing and mesh-to-mesh transfer scheme to simulate the cutting of such soft polycrystalline aggregates using a pseudograin model, with no restrictions on the friction, rake angle, or grain-size. Importantly, there is no need for a predefined separation line. The simulations successfully capture many experimentally observed aspects of the cutting of such 'gummy' metals, including sinuous flow, surface fold formation, thick mushroom-like type-I chips at low rake-angle, and thin, type-II chips with shear-plane like deformation at high rake-angle. The method also successfully replicates features like the formation of a stagnation zone ahead of the tool at high friction. Importantly, it permits accurate analysis of the cut surface, capturing the high strains, strain gradients, and deformed grain shapes in the wake of the tool. The presence of microstructure necessitates careful consideration of issues that do not arise in homogeneous remeshing simulations, including the need to model grain-splitting, grain-tracking, and mechanisms of material flow near the tool tip. The generality of the present approach makes it suitable to accurately model and simulate a wide range of machining processes.

Keywords: Simulation; microstructure; soft metals; remeshing;

1. Introduction

Accurate modeling and simulation of metal cutting processes is a problem of considerable practical significance for manufacturing, and has seen enormous efforts in the three decades since finite element (FE) analysis was first applied [1] to model orthogonal machining. While increased computational power and widely-available FE codes have aided analysts

---

*Assistant Professor; Corresponding author.
Email address: nsundaram@iisc.ac.in (Narayan K. Sundaram)

in simulating machining processes [2, 3, 4, 5, 6], it is recognized that the severe conditions concomitant with metal cutting – large plastic deformation with failure, high temperatures, and high strain-rates – still inhibit the quality and predictive ability of simulations [7, 8]. In particular, accurate material constitutive models [9] and interfacial (friction) models have long been identified as areas for improvement, and attracted considerable attention from the machining community (for a review, see [10]).

However, another important factor – the spatially inhomogeneous, polycrystalline aggregate nature of metals – is now attracting increasing interest in modeling and simulation. In recent years, a growing body of evidence from high-speed, *in situ* imaging experiments [11, 12, 13] shows that even in ductile, single-phase metals like commercially-pure (CP) aluminum and copper, the grain structure can dramatically alter cutting forces and chip type by promoting complex plastic flow modes, and also affect the quality of the machined (residual) surface. The aforementioned complex plastic flow modes are characterized by large and unsteady cutting forces, an extremely sinuous plastic flow pattern, thick continuous chips, and significantly damaged residual surfaces. These thick chips[1] were detected in earlier *post-mortem* studies [14, 15] as well, although the mechanism of their formation was unknown. Similar evidence has emerged in deformation processing [16], where homogeneous models that ignore microstructure drastically mispredict the outcome of sliding.

While there have been some attempts to incorporate simple microstructure-based models in machining simulations using a predefined separation layer [17, 18, 19, 20], these studies considered multiphase materials like two-phase iron, AISI-1045 steel, and ferritic-pearlitic steel, which are much less ductile than soft metals like annealed copper. Furthermore, these analyses have largely been restricted to the incipient stage of chip formation [17, 18] or focus on cutting forces [20] rather than the flow kinematics or grain deformation. Very recently, Wang et al. [21] conducted a CPFE-based simulation of ultra-precision cutting of few-grain (oligocrystal) copper by a diamond tool using a Johnson-Cook failure model. However, this 1 micron length-scale study cannot capture the complex flow kinematics, e.g.

---

[1] Also called 'Type-I' chips in the 4-fold Nakayama classification [14] of continuous chip morphologies

sinuous flow seen at the important and qualitatively different 1 mm / sub-mm length-scale in experiments [11, 12, 13]. Moreover, the large value of the ratio of grain-size (about 10 μm) to depth-of-cut (300-500 nm) in [21] reduces the number of grains the tool interacts with during the cutting to just one or two.

In the 100 μm - mm length-scale, the cutting of polycrystalline copper and aluminum beyond the incipient stage has been simulated in a Lagrangian FE framework using a pre-defined separation layer and a simple, 'pseudograin' constitutive model [22]. While these simulations capture several aspects of sinuous flow and type-I chip formation, the use of a separation layer is limiting in many ways. For instance, it effectively limits the (maximum) grain size to the uncut chip thickness and thus precludes analysis of the machined surface. Similarly, it is difficult to accommodate larger coefficients of friction (e.g. $\mu = 0.5$) because of excessive element distortion along the tool-work interface. Lastly, as is well-known in homogeneous machining, the use of a predefined separation layer is a somewhat *ad hoc* way to achieve material separation, and has been criticized on that account [23, 24, 25].

There is thus a need for a general framework to machine highly ductile polycrystalline aggregates with the ability to accommodate extreme plastic flow and a range of potential chip formation mechanisms with no restrictions on the friction, grain-size, or cutting (rake) angle. This work presents a general and broadly applicable remeshing and mesh-to-mesh transfer scheme for this purpose. Notably, while remeshing has been used with considerable success to simulate homogeneous machining [24, 26, 27, 28, 29], accommodating the presence of microstructure and the accompanying complex plastic flows is a more challenging problem, demanding careful consideration or rethinking of many aspects of mesh generation and remeshing, contact handling, grain tracking, and grain splitting, for successful simulation.

2. Methods

2.1. Simulation overview

Fig. 1 shows a schematic of the FE setup at the beginning of the simulation. The (rigid) tool is held at an angle α relative to the metal workpiece and is kept fixed, while the
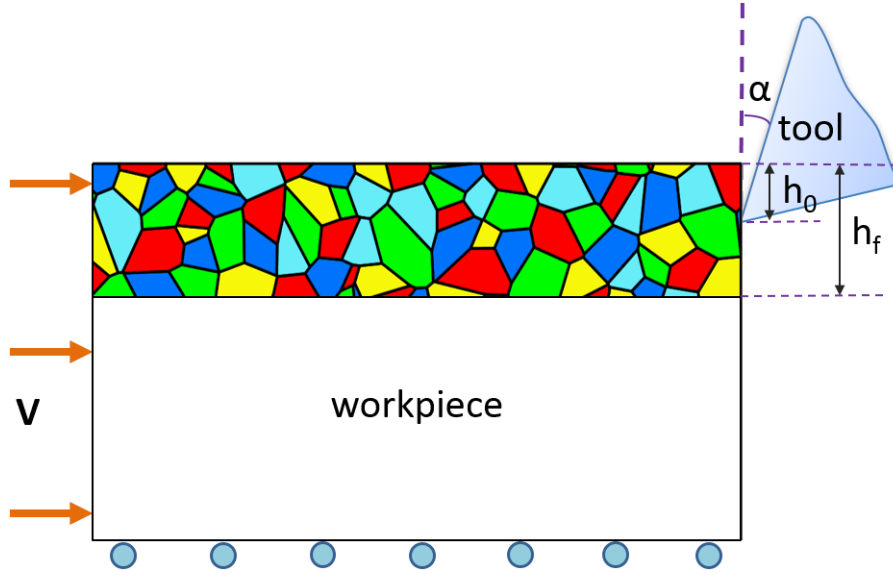
Figure 1: A schematic of the initial FE setup used for the remeshing simulations. α is the rake angle, h_0 the undeformed chip thickness and V the cutting speed. The region assigned a microstructure has depth h_f, which is typically about $4h_0$.

workpiece is pushed against the tool with a velocity V. The interaction depth / uncut chip thickness is h_0. The upper zone of the workpiece, of thickness h_f, is subdivided into idealized grains of mean size D using a pseudograin model [16]. Details of the pseudograin model and subdivision algorithm are given in [16], but the key idea is to assign slightly different plastic flow properties to each type or 'phase' of grain (grains of the same type have the same color in Fig. 1) to mimic the intrinsically inhomogeneous behavior of a polycrystalline aggregate arising from different grain-to-grain constraints and grain orientations [30, 31]. Note that there is no separation layer, and the subdivided zone extends well below h_0; h_f is typically about $4h_0$. For the present set of simulations, $V = 5$ mm/s, $h_0 = 125$ μm, and $D = 135$ μm. Two different values of the rake angle α are used, namely, $\alpha = 0.5°$ and $\alpha = 45°$.

Note that it is necessary to introduce a tool tip radius R_{tip} in a remeshing scheme : A value of $R_{tip} = 15$ μm is used in the present work. This value balances computational cost and accuracy; R_{tip}/h_0 is small enough (~ 0.12) so as to not affect the results significantly, but large enough to avoid extremely small near-tip elements.

The first step in running a cutting simulation involves generation of an initial microstruc-

ture and mesh. An FE solver is then invoked to step the simulation forward in time, with the analysis halted when a remeshing criterion is satisfied (see Sec. 2.2.2). The remeshing is followed by a mesh-to-mesh transfer of variables and grain tracking to update the microstructure in the deformed configuration, after which the simulation is resumed. This solve-remesh-map cycle is repeated as many times as required. Each of these individual operations is described in detail in the following sections.

2.2. Mesh generation and remeshing

2.2.1. Generation of initial mesh and microstructure

First, an initial microstructure of specified grain size D is created using a Voronoi tessellation process (see [32] for a survey), yielding a set of polygonal grains separated by grain boundaries; these grain boundaries are subsequently seeded for mesh generation. The density of seeds is higher for near-surface / near-tool grains, and decreases in a graded way toward the lower end of the specimen. It is important to note that since grain edges do not remain straight during deformation, they must be seeded with a sufficient number of points to enable accurate grain boundary tracking (see Sec. 2.3.1). Finally, one has a set of grains defined by the coordinates of points along grain boundaries and the specimen boundary. These coordinates are supplied to an open-source meshing code, Gmsh [33, 34], which has the ability to mesh polygonal regions.

A portion of a typical initial mesh / microstructure is shown in Fig. 2 (A more detailed view of the mesh, at three different magnifications, is shown in Supplementary Fig. S1). Note that the generated mesh conforms to the grain boundaries; neighboring grains also share nodes along grain boundaries to ensure continuity. The mesh itself consists entirely of bilinear, quadrilateral, plane-strain elements with a single Gauss quadrature point (reduced integration). A small fraction of the elements are necessarily degenerate quadrilaterals. The number of elements in the initial mesh varies from 7850-11000 in different simulations. This corresponds to an element size of $\sim$ 2-34 μm in the subdivided / microstructure layer of the initial mesh. However, due to adaptivity in the remeshing phase, the number of elements increases as the simulation progresses (see Sec. 2.2.3).
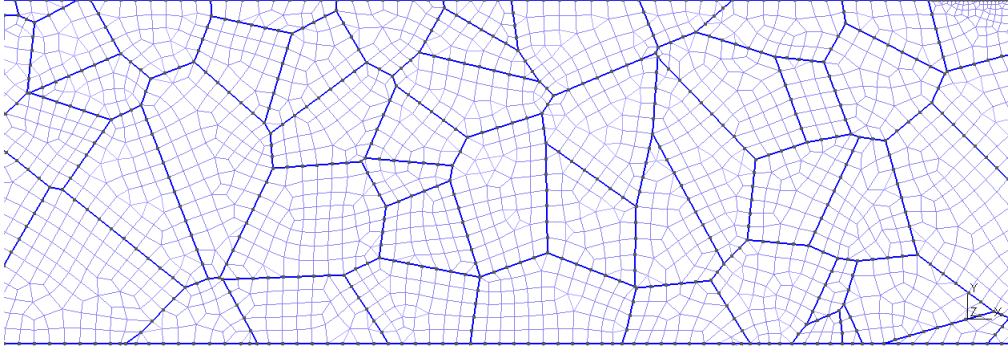
5

Figure 2: A portion of the initial mesh and microstructure; the mesh conforms to the grain boundaries.

2.2.2. Remeshing criterion

The selection of a remeshing criterion demands care, because infrequent remeshing can result in low solution quality and premature termination of the analysis. On the other hand, remeshing and mesh-to-mesh transfer is computationally expensive and associated with a small amount of diffusion, so that unnecessary remeshing is undesirable. Notably, in the presence of highly sinuous flow and self-contact formation, commonly used remeshing criteria like the element distortion criterion [4] and the maximum plastic strain increment criterion [24] are inadequate. Instead, the decision to remesh is based on a combination of contact interpenetration and element distortion in the present work: This entails stopping the analysis if contact interpenetration exceeds ∼0.3 microns, or if neighboring elements anywhere in the mesh penetrate each other due to mesh distortion. The analysis is then terminated and resumed from the *previous* output step, with the mesh in that step replaced by a new mesh. This heuristic procedure works quite well, balancing solution accuracy and computational cost.

2.2.3. Remeshing and adaptivity

Like the initial mesh generation, the remeshing process is also carried out grain-wise. The deformed grain boundaries are first obtained by a process described in Sec. 2.3.1. Remeshing is restricted to regions of the specimen which have an (absolute) $\bar{\varepsilon}$ value of 0.25 or higher; this avoids remeshing grains where there is little to no deformation, e.g. in regions distant from the tool tip.

Note that some regions of the mesh require a high element density. These include regions near the tool-workpiece contact and surface self-contact, as shown in Fig. 3. For instance, the mesh density must be adequately high near the tool-tip (Fig. 3a), failing which the contact pair algorithm can cause penetration of the workpiece by the tool and prematurely trigger the next remeshing. Similarly, self-contact regions (Fig. 3b) require a high element density to prevent interpenetration and accurately determine the self-contact pressure.

Lastly, it is desirable to have fine meshes in regions with high strain-gradients. In these cases, mesh refinement is achieved by increasing the number of seed points along the boundaries of grains that require refinement. New seed points are obtained by linear interpolation of existing seed points on the grain boundary. This is effectively an h-refinement process (see [35]). Overall, the remeshing / adaptivity process in the current work leads to a gradual increase in the number of elements as the simulation proceeds. The final (deformed) configuration of the workpiece has at least 3 times as many elements as the initial mesh; this ratio is as high as 7 for high friction simulations. The adaptive refinement also leads to element sizes as small as $\sim 0.3~\mu$m.
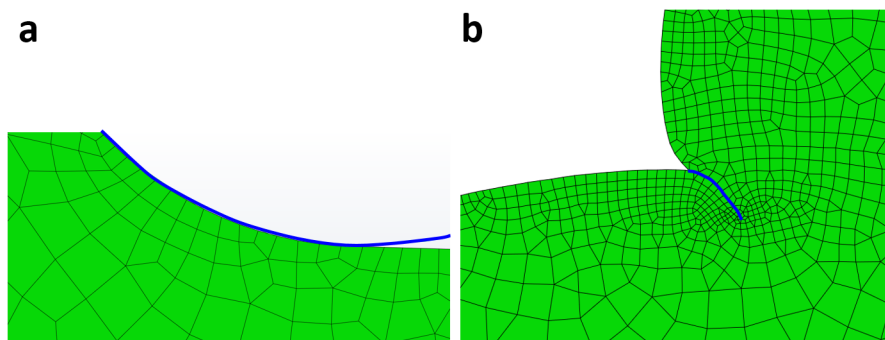

Figure 3: (a) Fine mesh in the workpiece along the tool radius to delay interpenetration and (b) Mesh refinement along self-contact

2.2.4. Mesh-to-mesh mapping of variables

A weighted average method is used to map solution variables from the old mesh to the new mesh. (For a survey of mapping schemes, see [36]). These variables include the stress components $\sigma_{xx}, \sigma_{yy}, \sigma_{xy}, \sigma_{zz}$, and effective plastic strain $\bar{\varepsilon}$ at the integration points, and

velocity components v_x, v_y at the nodes.

Let G^{h+1} denote a Gauss point in the new mesh M^{h+1}. The solution value at G^{h+1}, V_G^{h+1} is then calculated as [36]:

$$V_G^{h+1} = \frac{\sum_{i=1}^{N} w^i V_i^h}{\sum_{i=1}^{N} w^i} \tag{2.1}$$

Here V_i^h is the known solution value at the Gauss point G_i^h in the old mesh, N is the chosen number of Gauss points (which can be varied as required), and w^i is the weight function. A typical weight function is of the form $w^i = \dfrac{1}{d_i^n}$, where d_i is the distance between G^{h+1} and G_i^h, and n is a suitably chosen integer. A similar procedure is followed for nodal variables.

2.3. Grain handling

Accurate handling of grains in the microstructure is critical to successfully simulate polycrystalline aggregate cutting with remeshing, and it involves several important aspects which are discussed below. (These considerations are obviously not present in homogeneous FE with remeshing.)
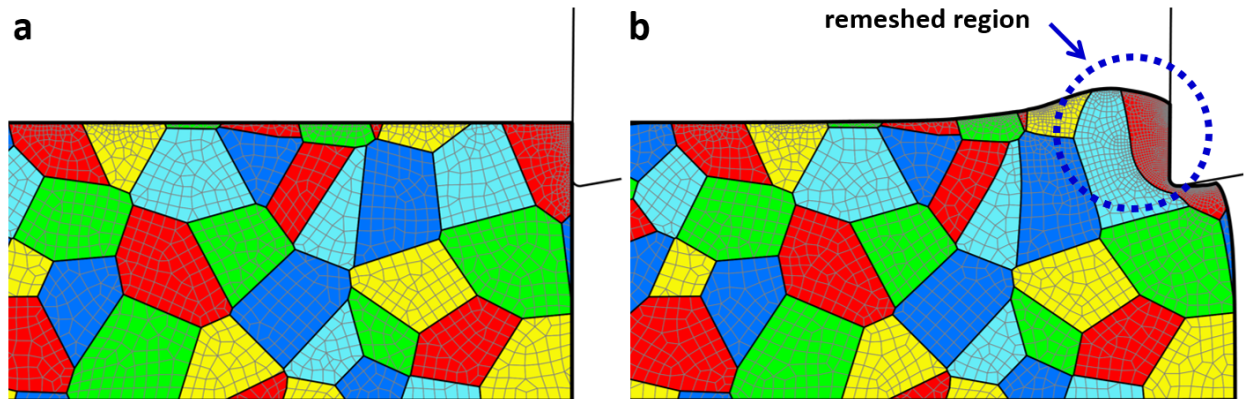
2.3.1. Grain boundary tracking

Figure 4: (a) Initial mesh (b) Mesh after a few remeshing steps. The mesh always conforms to the grain boundaries, whose evolution is tracked during the analysis. Notice the adaptivity and spatially selective nature of the remeshing process.

The basic FE paradigm involves elements and nodes only; as a result, grain boundaries must be tracked separately as the analysis proceeds. This is essential to ensure that material

initially identified as belonging to a particular grain (and therefore phase) retains the same plastic flow properties throughout[2]. It is also essential to ensure that the grain boundary geometry is not altered by the remeshing process itself, i.e. it should be the same just prior to and after a remeshing.

Fig. 4 shows the initial mesh (panel **a**) and the mesh after a few remeshing steps (panel **b**). Elements are color-coded to show their plastic flow properties. The grain boundaries in panel **b** are obtained by tracking the initial grain boundaries in panel **a** as the material deforms. This figure also highlights the adaptivity process discussed earlier, i.e., an increase in mesh density as material nears the tool-tip and the spatially selective nature of the remeshing. Note that there is a corresponding increase in the seed density along the grain boundaries in these adaptively remeshed regions.

2.3.2. Grain splitting

One important consideration in the cutting of polycrystalline aggregates is the possibility than an initially monolithic parent grain can split into two grains, one of which goes into the chip, and the other into the residual (cut) specimen surface. *In situ* experiments with a special etching process to highlight grains show precisely this kind of transgranular failure [11, 12]. Due to high ductility in annealed soft metals, the grains are also stretched extensively prior to splitting. Indeed, it is reasonable to consider that individual grains deform up to rupture (see discussion in Sec. 4.1). The problem of grain splitting then reduces to detecting an impending split and creating new grain boundaries; no explicit ductile failure criterion is required. Such a grain splitting scheme is shown in Fig. 5. Here grain 1 is the grain nearest to the tool-tip, and grain 2 represents a grain adjacent to grain 1. When the perpendicular distance between the tool tip and the narrowest region of grain 1 is smaller than a specified threshold (typically 2 μm), grain 1 is cut along the lines a-b and c-d to produce two (new) grains, 1a and 1b. These new grains inherit the plastic flow properties of the parent grain. Note that the lines a-b and c-d need not always be horizontal as shown in Fig. 5; these lines can also be inclined, e.g. a-b can have a slope equal to the slope of the

---

[2]This is obvious when one considers that grain boundaries are Lagrangian (material) features

grain 1: grain nearest to the tool tip
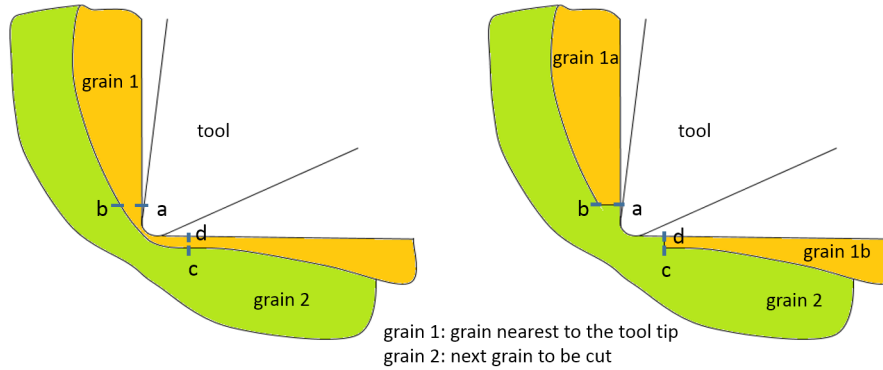grain 2: next grain to be cut

Figure 5: Simplified schematic of grain splitting. The grain nearest to the tool tip (grain 1) is allowed to split into grains 1a and 1b. The line $a - b$ need not be straight, and can have a slope equal to the slope of the grain edge nearest to the tool-tip.

segment of grain 1 nearest the tool-tip. In order to minimize the error in conserving grain phase volume, a-b and c-d are taken as close to the tool-tip as possible. Obviously, mesh density considerations set a lower bound on the lengths a-b and c-d. While heuristic, this splitting algorithm works quite well and seems reasonable on physical grounds. For instance, improper selection of the line a-b causes material assigned to grain 1a in the chip to flow again towards the cut surface, thus providing a mechanism to correct the location of a-b.

2.4. Constitutivity and contact model

The workpiece material in the present work is annealed OFHC copper, a representative single-phase ductile metal. Its elastic properties are E = 112 GPa and ν = 0.34. As mentioned in Sec. 2.1, a pseudograin model is employed to model microstructure-related inhomogeneity, with different plastic flow properties for each grain type / 'phase'. Conventional von Mises (J_2) isochoric metal plasticity is used to model individual phases in the workpiece, with isotropic hardening. Room temperature flow stress data for bulk OFHC copper is taken from [37], as are rate-dependent yield stress ratios. This bulk flow curve is shown in supplementary Fig. S3a; the rate-dependent yield stress ratios are shown in supplementary Table S1. For simplicity, the strain rate-dependence and elastic properties of the different phases are assumed to be identical.

Next, the flow curves for softer and harder phases in the polycrystalline aggregate are

10

obtained by scaling the bulk flow stress curve by a set of constant scale factors r_Y, with each one representing a ratio of the initial yield stress of that phase to the bulk yield stress, i.e. $r_Y = \sigma_Y^{phase}/\sigma_Y^{bulk}$. These scaled flow curves are shown in supplementary Fig. S3b. These phases are distinguished using color-coding in the present work (e.g. see Figs 1,4). A total of five phases are used; the values of r_Y for these five phases and their corresponding color codes are 1.12 (red), 1.06 (blue), 1.00 (green), 0.94 (yellow) and 0.87 (cyan). Here, 1.12 corresponds to the hardest phase and 0.87 the softest. This selected range of r_Y is a conservative one, and consistent with recent nanoindentation studies of individual grains in annealed FCC metals [38].

A master-slave, contact-pair algorithm is used to model contact between the tool and the workpiece[3]. Contact constraints are enforced kinematically. Self-contact is allowed along the free surface of the workpiece. A capped Coulomb friction model with maximum interfacial stress is chosen. Three values of the friction coefficient μ, namely, $\mu = 0.5$, $\mu = 0.3$, and $\mu = 0.1$ are used for this set of simulations, representing different extents of lubrication. Note that simulations with $\mu = 0.5$ or $\mu = 0.3$ cannot be run in a typical Lagrangian FE framework with a predefined separation line (see Sec. 4.1). The capping shear stress at the interface τ_{max} is 37500 psi ($\sim$258 MPa) in all cases.

2.5. Solver and postprocessing

The Abaqus explicit dynamics solver is used in all simulations. An explicit dynamics integration scheme is chosen largely because the handling of contact boundary conditions is more robust [39, 40]. Specimen elements are suitably mass-scaled to increase the stable time increment and decrease computational time, using a combination of fixed and variable mass-scaling. It is ensured that the kinetic energy is significantly less than 5% of plastic dissipation for most of the simulation, so that the response is not dominated by inertia. Due to the low cutting speed modeled in the present work, as well as the very high thermal diffusivity of OFHC copper, it is sufficient to conduct an isothermal, stress-only analysis.

---

[3]For self-contacts, a balanced contact-pair algorithm is used.

Since grain boundary nodes are tracked during the cutting, they act as a set of Lagrangian tracers. However, to obtaining additional flow information, e.g. streaklines, a rectangular grid of Lagrangian tracer particles is constructed in the undeformed mesh at the start of the simulation. This grid of material points is also tracked as the cutting proceeds; the tracking uses linear interpolation of the deformation field as well as coordinates of the edges of the grains.

Table 1: Simulation parameters

Simulation #	1	2	3	4
V	5 mm/s			
h_0	125 μm			
h_f	535 μm			
Workpiece	OFHC Cu			
Mean grain size D	135 μm			
α	0.5°	0.5°	0.5°	45°
Workpiece size	5.3 mm x 2.8 mm	5.3 mm x 2.8 mm	7.5 mm x 3.6 mm	5.3 mm x 2.8 mm
No. of elements	7850 - 46400	7850 - 55600	11000 - 32800	7850 - 20100
μ	0.5	0.3	0.1	0.1
τ_{max}	37500 psi ($\sim$ 258 MPa)			

3. Results

The remeshing framework presented in the preceding section allows cutting of ductile polycrystalline aggregates under a wide range of conditions. Results from four such representative simulations are presented here. A summary of the simulation parameters is given in Table 1.

3.1. Development of sinuous flow at high friction

Fig. 6 shows four snapshots (panels **a-d**) from a Cu cutting simulation at $\alpha = 0.5°$ and a high μ of 0.5. The snapshots are taken at times t = 0.20 s, 0.22 s, 0.32 s and 0.43 s,
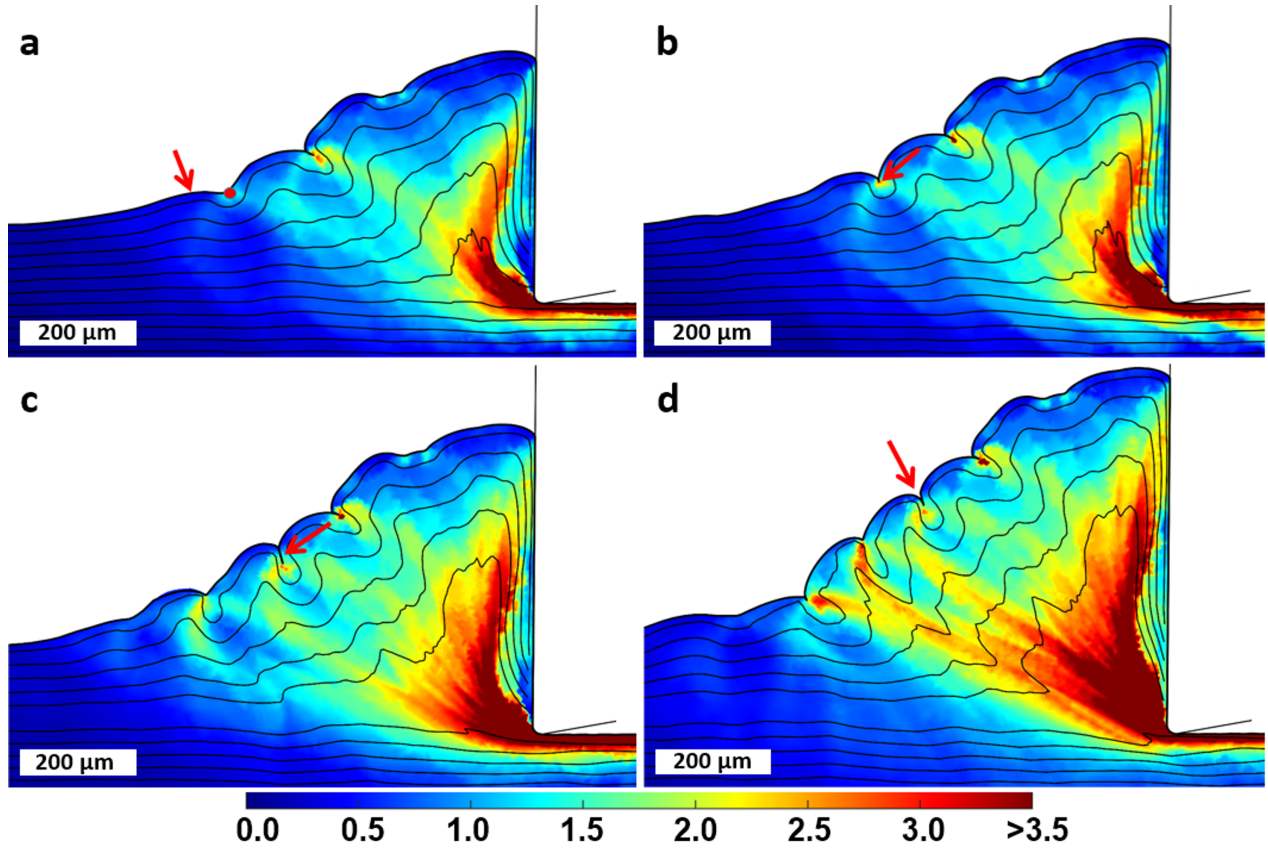
Figure 6: Four frames (a-d) from a Cu cutting simulation showing the development and attributes of sinuous flow. The snapshots are at times $t = 0.20$ s, 0.22 s, 0.32 s and 0.43 s. The streaklines of flow are highly undulating or sinuous. The back side of the chip has several folds with mushroom-like appearance (Type-I chip), a typical attribute of sinuous flow. The chip root is shown by the circular marker in panel (a). A bump nucleates at the chip root (a). The bump forms a self-contact with the material in the chip (b). Subsequently, the self-contact lengthens as shown in (c) defining an edge of the fold. The process repeats at the other edge, defining another edge of the fold. The background color in each panel depicts $\bar{\bar{\varepsilon}}$. The simulation parameters are $\alpha = 0.5°$, $V = 5$ mm/s, $h_0 = 125$ μm, $D = 135$ μm

corresponding to cut lengths of 1 mm, 1.1 mm, 1.6 mm, and 2.15 mm respectively.

Notably, cutting this soft single-phase metal causes a sinuous flow pattern to develop: This is visible from the highly undulating streaklines of flow (with maximum peak-to-valley amplitudes of 105, 109, 128, and 130 microns in panels **a**, **b**, **c**, and **d** respectively). In addition, there are numerous folds on the back side of the chip giving it a characteristic mushroom-like appearance. There are four stages of development of the sinuous flow, as

13

seen in Fig. 6; from the initiation of a bump near the chip root (red arrow in panel **a**), to the formation of a self-contact / fold (panel **b**) to its subsequent growth (panel **c**). Because the chip is still developing at this stage, the separation of the self-contact due to hydrostatic tension in the backside of the chip is still underway in panel **d**.

The sinuous flow is characterized by a highly spatially inhomogeneous $\bar{\varepsilon}$ field in the chip (background color), as seen in panel **d**. For instance, near the tool tip, $\bar{\varepsilon} \approx 6.0$. At the back of chip, the roots of self-contacts have strains as high as 3.0, while the mushroom-like fringes along the back side of the chip have strains as low as 0.4. The mean chip strain is 1.77, 1.88, 1.88, and 2.33 respectively in panels **a-d**.

One important characteristic of this high-friction cutting simulation is the development of a stagnation zone just ahead of the tool and for some distance along the tool face. This can be deduced from the fact that streaklines of flow terminate in this region, indicating accumulation of material there. An examination of the velocity field v in this region also confirms that $|v|/V < 0.05$. Such zones have also recently been observed in *in situ* experiments in annealed Al-1100, with a very low velocity region ($|v|/V < 0.05$) seen to develop near the tool tip (Private communication from Dr. Tatsuya Sugihara, Osaka University).

Notice that the chip is still growing in panel **d**. This is because the cutting distance required to reach a potentially steady thickness is infeasibly long at this high value of μ; in fact the chip is yet to begin to curl away from the tool face at $t = 0.43$ s.

Fig. 7 shows two snapshots of the deformed grain pattern / microstructure from this simulation. These snapshots are taken at times $t = 0.20$ s (panel **I**) and 0.43 s (panel **II**). It is instructive to track a few select grains as they deform. Consider the two neighboring surface grains, **a** and **b** in panel **I**. After deformation, both these near-surface grains are stretched and elongated to a considerable extent in the chip thickness direction and compressed in a direction perpendicular to it. As a result, the aspect ratios of these initially boxy grains become as high as 9.1 and 9.3 after deformation (panel **II**). This feature reflects large plastic strains and intense shearing in the development of type-I chips.

Notably, both these grains flow into the chip after cutting. Of more interest are the two subsurface grains labeled **c** and **d** in panel **I**; portions of these grains lie at a depth
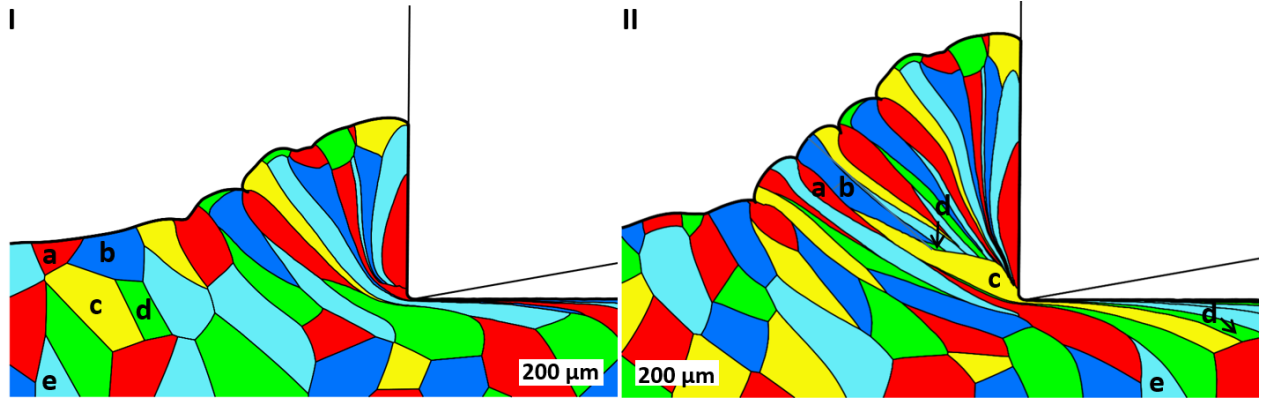
Figure 7: Two snapshots from a Cu cutting simulation at $t = 0.20$ s and $t = 0.43$ s showing grain deformation in sinuous flow. The grains **a** and **b** in (I) are only lightly deformed. The corresponding deformed picture of **a** and **b** is shown in (II), where these grains are severely stretched and rotated. The grain **c** is about to be split in panel (II). Grain **d** in (I) splits into two pieces in (II), with the majority of its mass flowing into the cut surface. The grain **e** in (I) flows entirely into the specimen (II). The simulation parameters are $\alpha = 0.5°$, $V = 5$ mm/s, $h_0 = 125$ μm, $D = 135$ μm, $\mu = 0.5$

greater than h_0 at the beginning of the simulation. Grain **d** is monolithic in panel **I**, but is (subsequently) split between the chip and the residual (cut) surface in panel **II**. The new, split grains are indicated in panel **II**. It is notable that the cut fragment that flows into the residual surface is highly sheared; this constitutes the bulk of the grain mass. A much smaller fragment flows into the chip.

Grain **c**, which is initially adjacent to **d**, is just about to be split in panel **II**. After splitting, the mass of this grain would be shared nearly equally between the chip and the residual surface. Lastly, grains like **e** in panel **I** lie well below the tool tip, and flow entirely into the specimen. While grain **e** is sheared somewhat, it is deformed to a much smaller extent than the grains that flow into the chip or are split during the cutting.

It is also instructive to examine the plastic strain rate field in this simulation. Fig. 8 shows two snapshots of the strain rate $\dot{\bar{\varepsilon}}$ taken at times $t = 0.24$ s (panel **a**) and 0.36 s (panel **b**). These strain-rate fields show certain characteristics which are quite distinctive: First of all, there is no distinct shear plane; the active deformation zone is wide and diffuse, although there is a jet-like region of high strain rate emanating from the tool tip. Since
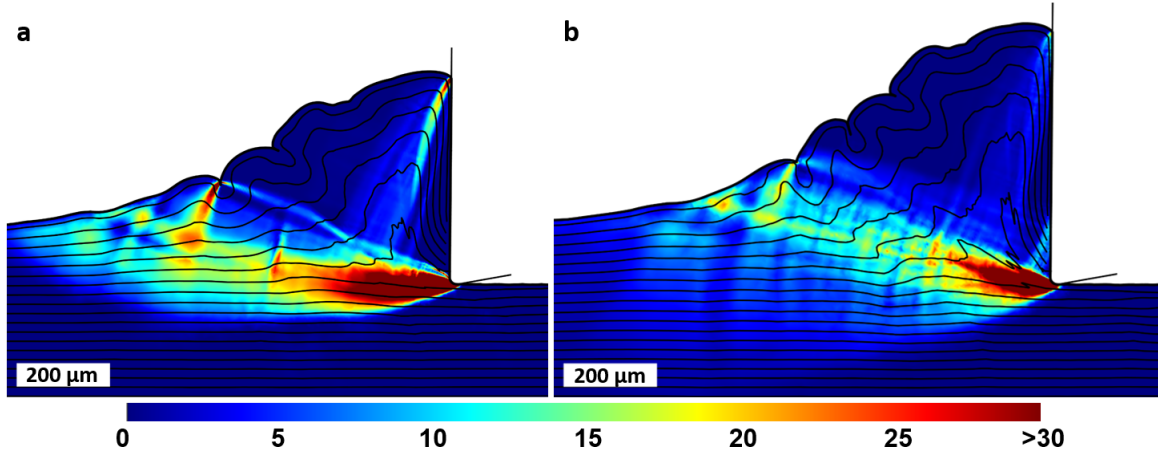
15

Figure 8: Two frames from an FE simulation at $t = 0.24$ s and 0.36 s. The background color shows the plastic strain rate $\dot{\bar{\varepsilon}}$ (units of s^{-1}). No distinct shear plane is observed. Characteristic of sinuous flow, panel (a) shows a transient, high-strain-rate fringe near a fold root, which disappears in panel **b**. The simulation parameters are $\alpha = 0.5°$, $V = 5$mm/s, $h_0 = 125$ μm, $D = 135$ μm, $\mu = 0.5$

the chip is still growing, the direction of this high strain-rate jet also rotates from nearly horizontal in panel **a** to a somewhat acute angle (13°) directed into the chip in panel **b**. Because of self-contact formation, the strain rate field shows many transient features, e.g. panel **a** shows an additional fringe of high strain rate emerging from a fold root, which disappears subsequently (panel **b**).

3.2. Cutting response at intermediate and low friction

Fig. 9 shows two snapshots (panels **a** and **b**) from another Cu cutting simulation at $\alpha = 0.5°$, which has a somewhat lower $\mu = 0.3$, but is otherwise identical to the first simulation. These snapshots are taken at times t = 0.31 s and 0.50 s, corresponding to cut lengths of 1.57 mm and 2.54 mm respectively. As in the $\mu = 0.5$ simulation in Fig. 6, there is considerable sinuous flow, and folding / self-contact formation at the surface. The maximum sinuous flow amplitude is 105 μm in panel **a** and 150 μm in panel **b**. The $\bar{\varepsilon}$ field (background color) is again highly inhomogeneous.

However, there are important differences with the $\mu = 0.5$ simulation. Owing to the lower friction, the development of the chip is more pronounced at these cut lengths. This is reflected in the fact that the chip starts to curl away from the tool tip in Fig. 9**b**. Moreover,
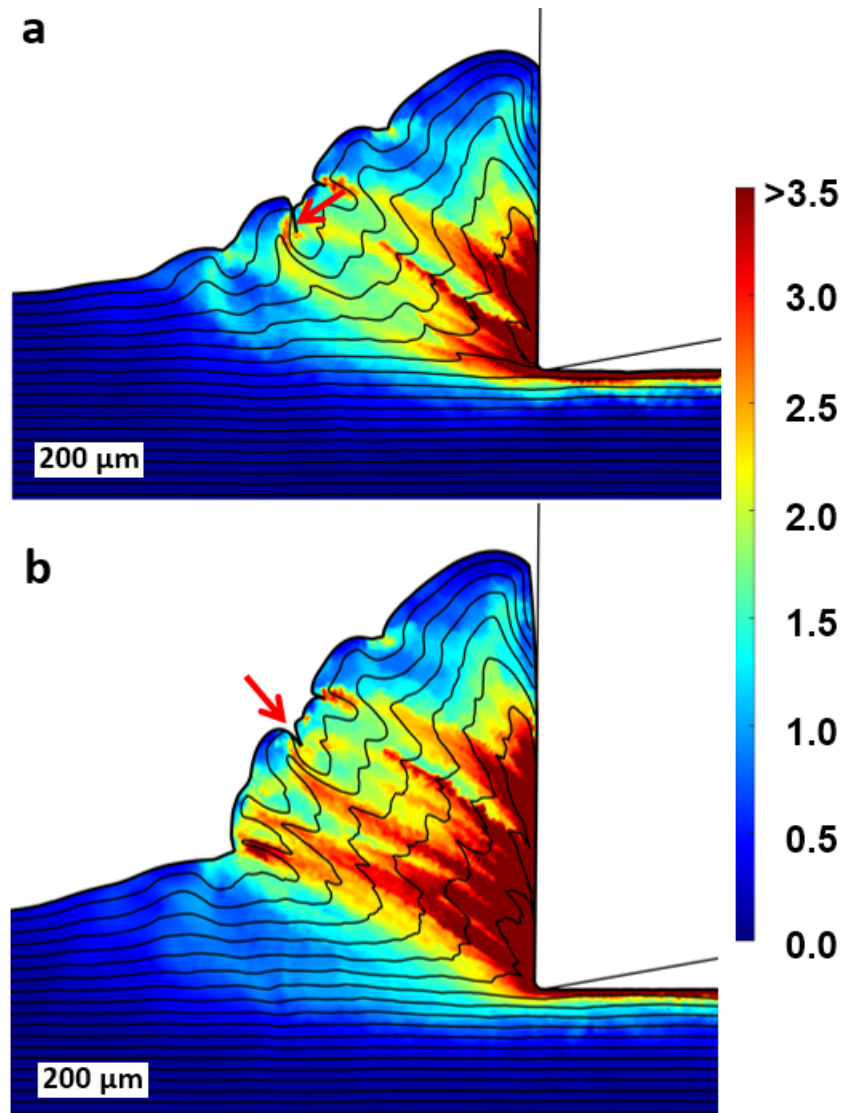
16

Figure 9: Two frames from a Cu cutting simulation with $\mu =0.3$ and $\alpha = 0.5°$ at times $t = 0.31$ s (a) and 0.50 s (b). Notice the chip curl in frame (b), in contrast to the simulation with $\mu = 0.5$. The self-contact shown by the red arrow in (a) opens up in (b). The background color in each panel depicts $\bar{\varepsilon}$. The simulation parameters are $\alpha = 0.5°$, $V = 5$ mm/s, $h_0 = 125$ μm, $D = 135$ μm

unlike the $\mu = 0.5$ simulation, there is no stagnation zone near the tool tip: Streaklines of flow terminate high in the chip instead, indicative of the fact that material is transported up along the rake face instead of accumulating ahead of the tool tip. The mean chip strain is about 3.01 in panel **a** and about 3.29 in panel **b**; the corresponding mid-thickness chip strains are 1.66 in **a** and 2.01 in **b**. The chip thickness and mushroom-like backside clearly

identify it as a type-I continuous chip in the Nakayama classification [14]. Lastly, the self-contact in panel **a** (red arrow) is seen to open up in panel **b**, indicating the presence of a tensile stress field at the back of the chip.

The corresponding grain deformation pattern, shown in Fig. 10 (also see supplementary movie M1), is again characterized by the elongation of grains into thin, high-aspect ratio shapes in the chip. Of interest is the fact that single, near-surface grains like grain **a** in panel **I** can span the entire thickness of the chip (panel **II**). Due to this, a portion of a surface grain like **a** can interact surprisingly closely with the cutting edge of the tool. Also of note is grain **c** which flows largely into the cut surface, with only a small sliver incorporated into the chip. This is in contrast with grain **c** in Fig. 7, which is shared nearly equally between chip and cut surface. This demonstrates the ability of the present method to accommodate all possible grain splitting scenarios. Lastly, when μ is reduced to 0.1, sinuous flow is still
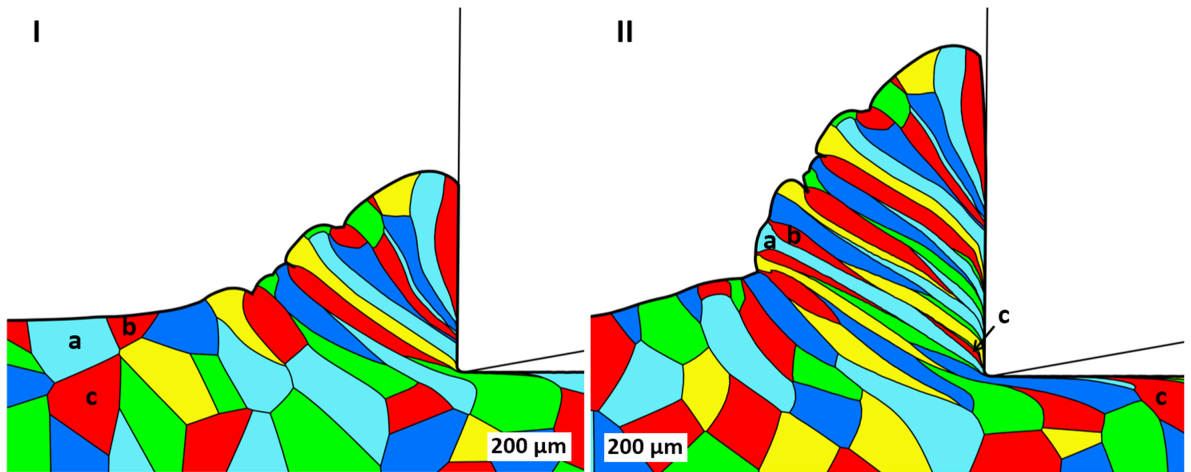

Figure 10: Two frames from a $\mu = 0.3$, Cu cutting simulation at $t = 0.22$ s (panel **I**) and $t = 0.50$ s (panel **II**) showing grain deformation. The grains **a** and **b** in (I) are only lightly deformed, but are severely stretched and rotated in the chip (panel **II**). Grain **c** is split between the chip and the cut surface (panel **II**), with the bulk of its mass flowing into the cut surface. The simulation parameters are $\alpha = 0.5°$, $V = 5$ mm/s, $h_0 = 125$ μm, $D = 135$ μm, $\mu = 0.3$

observed, but its extent is reduced: For instance, the peak sinuous flow amplitude is 45 μm, and the chip thickness is lower (see Fig. 14 for a plot of chip thickness evolution). Other features of sinuous flow, e.g. self-contacts, are present, but their amplitude is typically

smaller.

3.3. Effect of cutting geometry

The previous simulations were conducted at a rake angle of $\alpha = 0.5°$. Fig. 11a shows a snapshot from a simulation in which the rake angle is increased to $\alpha = 45°$, all other parameters being the same. The difference in flow pattern is dramatic: The sinuous flow is absent and the streaklines of flow are smooth and laminar. There are minor undulations on the free surface of the chip, but no self-contacts. The chip itself is much thinner (chip thickness ratio, $\lambda = h_c(t)/h_0$, where $h_c(t)$ refers to the instantaneous chip thickness, reaches a steady value of 1.6 in this case), with a mid-thickness chip strain of only about 0.58. The chip material next to the tool shows a layer of locally high strain ($\bar{\varepsilon}$ of 5 in the chip); the occurrence of this layer is discussed in the Sec. 4.3. The deformed microstructure in Fig. 11b shows chip grains which are only slightly deformed; the extreme changes in aspect ratio noted in the $\alpha = 0.5°$ simulations are absent.
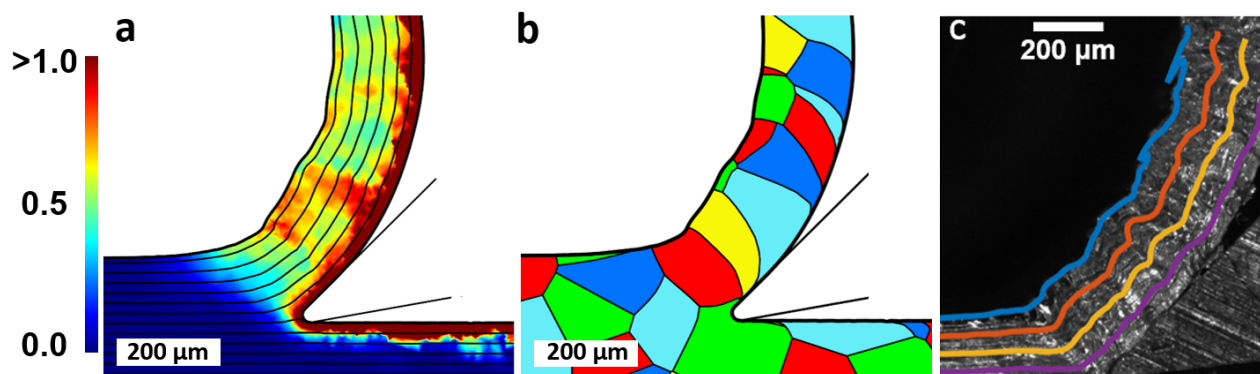

Figure 11: (a) Snapshot of $\bar{\varepsilon}$ from a Cu cutting simulation with $\alpha = 45°$ and $\mu = 0.1$ at $t = 0.2$ s. The streaklines of flow are laminar, in contrast with the $\alpha = 0.5°$ results. $V = 5$ mm/s, $h_0 = 125$ μm, $D = 135$ μm. (b) Deformed grains corresponding to the strain field in panel (a). (c) Snapshot from an experimental imaging study of low-speed cutting of annealed copper [11] at $\alpha = 45°$. There is excellent agreement between FE simulations and the experiment.

For comparison, Fig. 11c shows a snapshot from an *in situ* imaging experiment (from [11]) of low-speed cutting of annealed OFHC copper, with PIV postprocessing to obtain
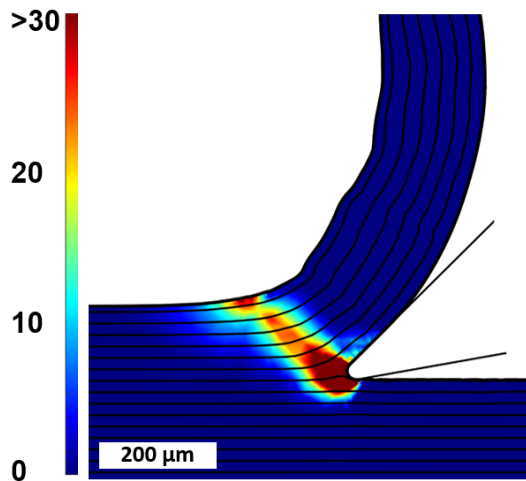
Figure 12: One frame from a Cu cutting simulation with $\alpha = 45°$ and $\mu = 0.1$ at $t = 0.2$ s, showing the plastic strain rate $\dot{\bar{\varepsilon}}$ (units of s$^{-}1$). The instantaneous deformation is concentrated along a band, which strongly resembles a 'thick' shear plane. The other simulation parameters are $V = 5$ mm/s, $h_0 = 125$ μm, $D = 135$ μm.

streaklines[4]. There is excellent agreement between the simulation flow patterns in panels **a** and **b**, and the experiments (panel **c**) in all aspects, including chip thickness ($\lambda \sim 1.8$), flow pattern, minor undulations on the free surface, chip curl, and so on.

The thin chip in Fig. 11a may be classified as a type-II chip in the Nakayama [14] classification (unlike the type-I chips associated with sinuous flow). This is corroborated by an examination of the plastic strain-rate field in Fig. 12. The instantaneous plastic deformation is spatially localized, extending in a band from the tip of the tool to the free surface at angle of 40° from the horizontal. This spatially localized narrow band of deformation may well be considered a shear-plane; Of course, the zone has a finite thickness of about 80 microns, which is likely on account of strain hardenability of the material and the finite (non-zero) tool-tip radius.

3.4. Cutting force and chip thickness

Fig. 13 shows the time evolution of the cutting force F_x for the remeshing simulations discussed in the earlier sections. The simulation with $\alpha = 0.5°$, $\mu = 0.5$ has the highest
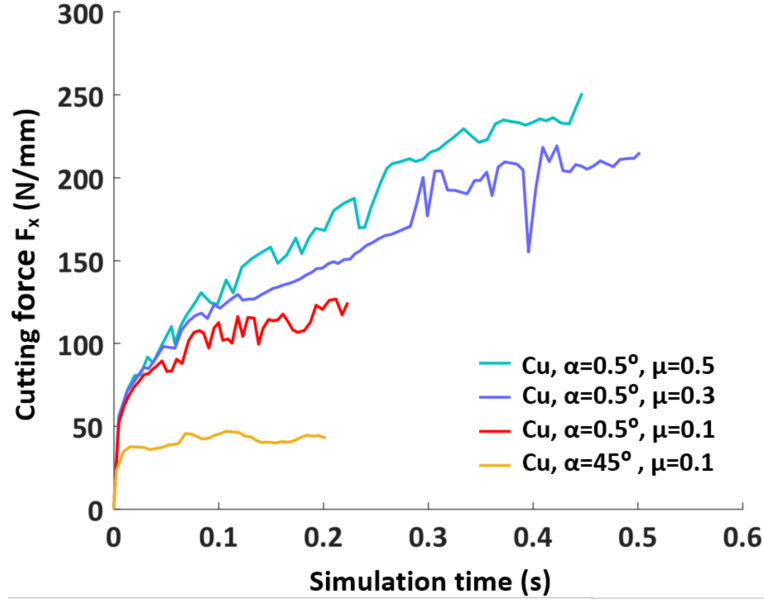
---

[4]See [11] for experimental details

Figure 13: Time evolution of cutting force F_x in FE simulations with remeshing. F_x reaches 250 N/mm for the simulation with $\alpha = 0.5°$ and $\mu = 0.5$ and 210 N/mm for $\alpha = 0.5°$, $\mu = 0.3$. There is a dramatic decrease in F_x when $\alpha = 45°$, $\mu = 0.1$. F_x becomes steady in this case, at about 43 N/mm

cutting force with a value of about 250 N/mm[5]; this value shows an increasing trend even at the end of the simulation, reflecting the fact that attaining quasi-steady conditions would require a much higher cutting distance. The $\alpha = 0.5°$, $\mu = 0.3$ simulation has a somewhat lower F_x throughout, reaching a value of about 210 N/mm at the end of the simulation. These cutting force curves are also marked by significant fluctuations. Notably, this value of cutting force compares quite well with the $F_x = 267$ N/mm (800 N / 3 mm) in [11] while cutting annealed OFHC copper under somewhat similar conditions.

The lowest cutting force occurs (as expected) for the simulation with $\alpha = 45°$ corresponding to 'laminar' flow and type-II chip formation. Moreover, it attains an approximately steady value of 43 N/mm; this is much smaller than even the 125 N/mm F_x for the $\alpha = 0.5°$, $\mu = 0.1$ simulation. Commensurate with the absence of surface self-contact formation, transient force fluctuations are quite small in comparison to all the $\alpha = 0.5°$ simulations.

_____

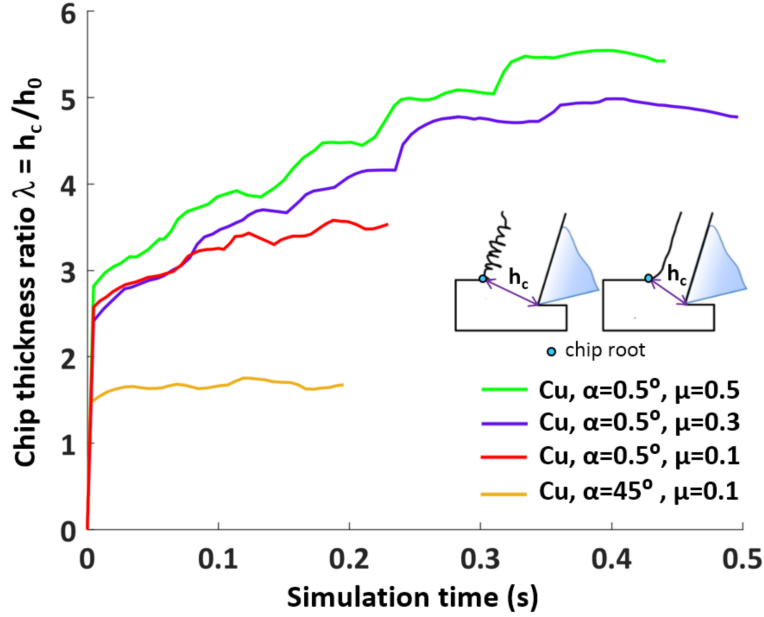[5]The force units are N/mm because these are plane strain simulations

Figure 14: Time evolution of chip thickness ratio $\lambda = h_c(t)/h_0$ in simulations corresponding to Fig. 13. The simulation with $\alpha = 0.5°$ and $\mu = 0.5$ develops the thickest chip ($\lambda \sim 5.5$). The chip thickness ratio reduces to 3.6 when μ is decreased to 0.1. The thinnest chip is obtained when $\alpha = 45°$, $\mu = 0.1$; a nearly steady value of $\lambda \sim 1.6$

A similar trend is observed in the corresponding plots of λ, as seen in Fig. 14. λ reaches a maximum of ~ 5.5 for the simulation with $\alpha = 0.5°$, $\mu = 0.5$ and about 4.98 when $\mu = 0.3$. With a lower μ of 0.1, λ decreases to about 3.6. Again, λ is expected to continue to grow further in these three simulations. For the simulation with $\alpha = 45°$, a much smaller, and steady λ of 1.6 is obtained.

3.5. Hydrostatic pressure in the chip

Fig. 15 shows the hydrostatic pressure field from the $\mu = 0.3$ simulation at $t = 0.50$ s; panels **a** and **b** are color-coded differently to highlight regions of tension and compression. The chip is well developed at this stage. Most of the chip is in compression, but there is evidently a zone of tensile hydrostatic stress at the back of the chip. This is in the form of a layer of variable thickness along the free surface of the chip. The roots of self-contacts (panel **b**) have the highest tensile hydrostatic stresses in the chip, of about 620 MPa. These tensile stresses result in opening up the faces of the self-contact in Fig. 9b. Large tensile
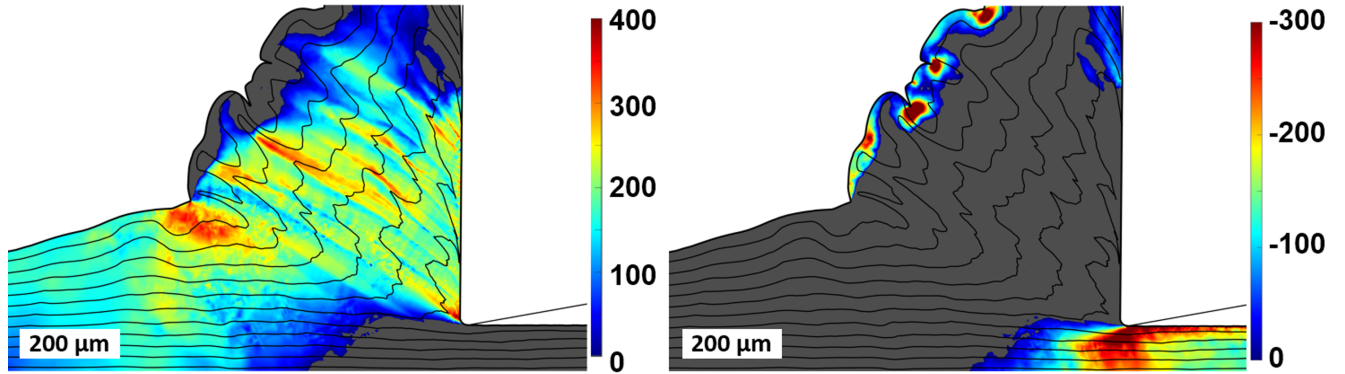
Figure 15: Snapshots from the $\mu = 0.3$, Cu cutting simulation taken at $t = 0.50$ s. The background color in both panels depicts the same hydrostatic pressure field (in MPa; tensile stresses negative), but are color coded differently to highlight compression in panel (a) and tension in panel (b). The simulation parameters are $\alpha = 0.5°$, $V = 5$ mm/s, $h_0 = 125$ μm, $D = 135$ μm, $\mu = 0.3$

stresses of $\sim$380 MPa also occur immediately behind the tool tip and just below the specimen surface.

4. Discussion

4.1. A general scheme for cutting ductile polycrystalline aggregates

The results in the preceding section show that the remeshing and mesh-to-mesh mapping scheme developed in the present work can be deployed to simulate the cutting of ductile polycrystalline aggregates under a wide range of conditions. For instance, analyses with higher values of friction (e.g. $\mu = 0.5$) can be simulated using the present approach. There is similarly no restriction on the grain size D or the rake-angle α.

Notably, the present scheme successfully captures the mechanics of grain deformation and splitting in such metals: This is illustrated in Figs. 16 and 17 below.
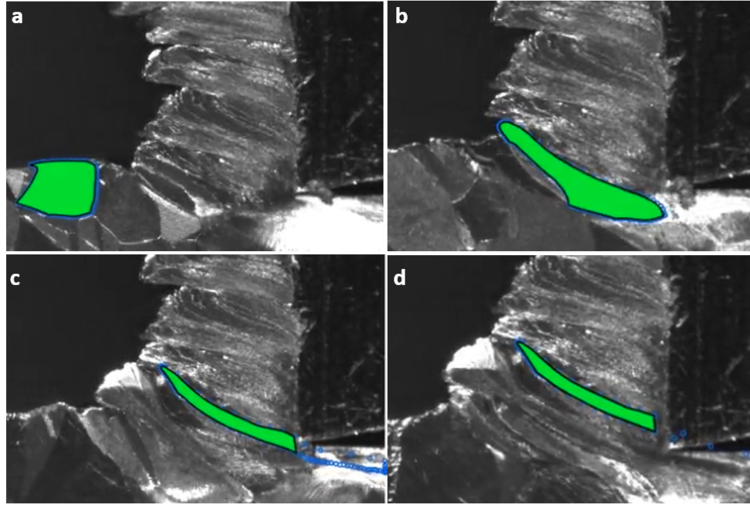
23

Figure 16: Four snapshots from an in situ imaging experiment depicting the deformation of a grain (shaded in green) during cutting of annealed OFHC copper; the grain evolves from a nearly undeformed boxy shape (a) into two elongated, high-aspect ratio daughter grains (d) in the chip and cut workpiece. The highly sheared daughter grain in the cut surface (c, d) is indicated by open circles. $\alpha = 0°$, $V = 0.5$ mm/s; a special etching process was used to highlight grains [12].
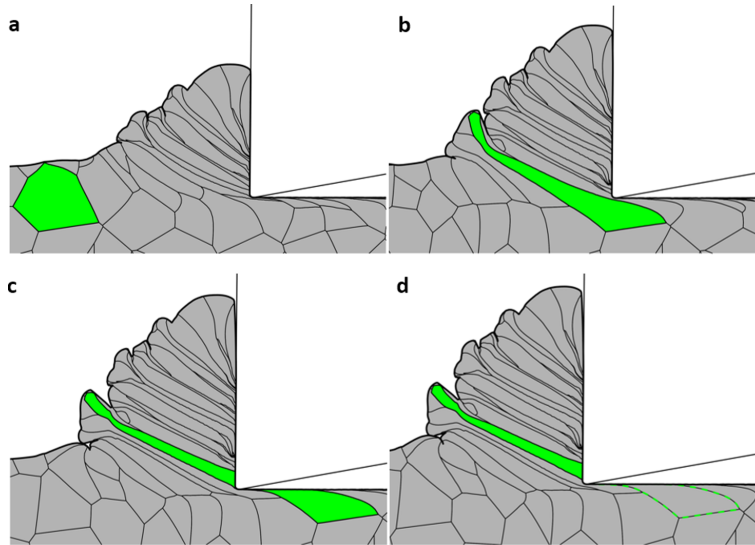

Figure 17: Four snapshots ($t = 0.32$ s (panel a), 0.49 s (panel b), 0.56 s (panel c) and 0.57 s (panel d)) from an OFHC copper cutting simulation showing the grains as they deform. The tracked grain (shaded in green) evolves almost exactly as seen in the experiments in Fig. 16. Simulation conditions: $\alpha = 0.5°$, $\mu = 0.3$, $V = 5$ mm/s, $r_y^{max} = 1.24$

Fig. 16 shows four frames from an *in situ* imaging experiment[6] of cutting of annealed OFHC copper at low speed, with a special etching technique to highlight grains [11]. As the cutting proceeds, an initially largely undeformed grain (shaded grain in panel **a**) is stretched and rotated (panel **b**) as it enters the chip. Portions of the grain then become progressively thinner near the tool-tip (panel **c**) before the grain finally splits into two (panel **d**; boundary of grain on cut surface indicated by open circles in panels **c** and **d**).

A nearly identical sequence of events is observed in our cutting simulations, as shown in Fig. 17, panels (**a-d**). As in the experiments, we track one particular grain (shaded in green) during the cutting process. There is clearly a very similar evolution in the grain shape during the cutting process, including the initial stretching and rotation, the process of splitting itself, and the high-aspect ratio daughter grains in the chip and on the cut surface. Notably, the present work allows grains to split as dictated by the flow mechanics, rather than by imposing a predefined separation line.

Beyond this striking similarity in the process of grain deformation and splitting, there is also close agreement between numerous aspects of the mechanics of deformation reported in the present work and experiments on soft metal cutting at the 100 μm to few mm length-scale. These features are summarized in Table 2 below, and include sinuous flow with highly undulating flow streaklines, surface fold formation, thick mushroom-like type-I chips, high aspect ratio grains in the chip, near-surface strain gradients indicated by differentially deformed grains in the cut surface at low rake-angle; and thin, type-II chips with laminar flow and low cutting force at high rake-angle. Many aspects of grain deformation in sinuous flow can also be seen in supplementary movie M1.

---

[6]Courtesy: Center for Materials Processing and Tribology, Purdue

Table 2: A comparison of features observed in soft polycrystalline aggregate cutting using simulations (the present work) and published experiments. The bolded text refers to figure numbers in the corresponding numbered references.

Observed feature	Simulations	Cutting experiments
'Sinuous' streaklines of flow	Figs. 6(a-d)	Fig. **1a** in [41]; Figs. **2a,3** in [11]
Characteristic mushroom like features on backside of type-I chip	Figs. 6(a-d), 7	Figs. **1b,1c** in [41], Fig. **2a** in [11], Fig. **16a** in [15], Fig. **3a** in [14], Fig. **2** in [42]
Bump formation at chip root prior to self-contact	Figs. 6a, 7a	Fig. **2a** in [41]
Formation of self-contacts	Figs. 7b, c	Figs. **3b, 3c** in [11]
Laminar flow / thin, type-II chips at high α	Figs. 11a, 11b	Fig. 11c in present work; Fig. **9a** in [11]
High λ and cutting force with sinuous flow	Figs. 6, 14, 13	Figs. **2,3** in [11], Fig. **3** in [13]
High aspect ratio grains in chip	Figs. 7, 10	Fig. **5** in [12], Fig. **10** in [11]
Residual surface strain profile	Fig. 18	Figs. **4,5** in [43] and Fig.**11** in [13]
Stagnation zone at high μ	Subsection 3.1	Subsection **2.3** in [44], Fig.**8** in [45]

4.2. Analysis of the cut surface

One of the advantages of using remeshing to simulate polycrystalline aggregate cutting is that it allows analysis of the cut surface – including accurate assessment of residual surface grains and surface strains – which cannot be done accurately when a predefined separation layer is used. Such an analysis of the machined surface is of primary importance in assessing its integrity [46, 47, 48].

Fig. 18a shows a snapshot from the Cu simulation with $\alpha = 0.5°$ and $\mu = 0.5$ showing the plastic strain $\bar{\varepsilon}$; the figure shows about 430 μm of the cut surface in the wake of the tool. There is evidently a high strain gradient at the cut surface, with the strain dropping
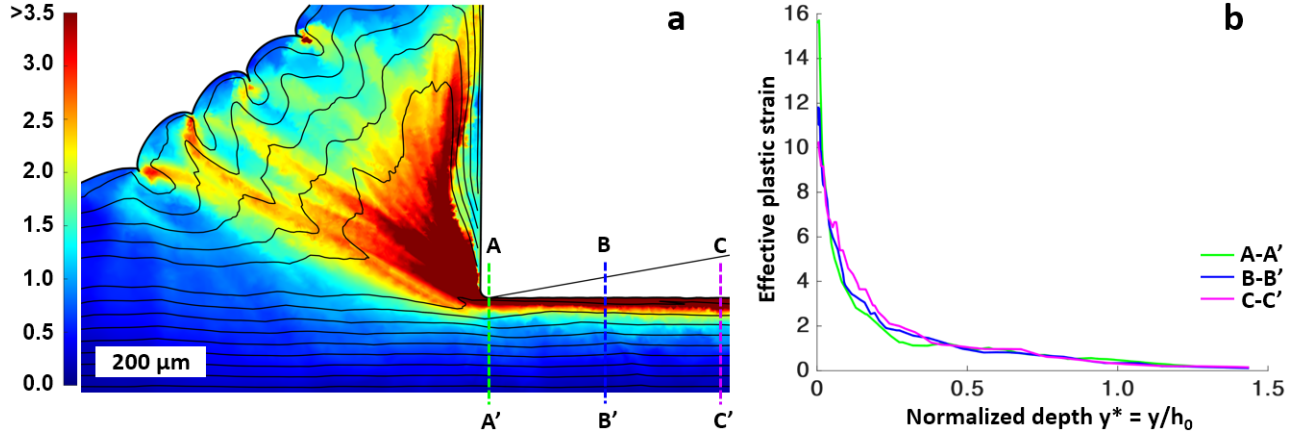
Figure 18: (a) Snapshot showing residual surface strain for a Cu cutting simulation with $\alpha = 0.5°$ and $\mu = 0.5$ at $t = 0.43$ s. Three locations are identified at the residual surface, namely, A-A', B-B' and C-C'. (b) Plots of effective plastic strain $\bar{\varepsilon}$ into the depth at the indicated locations. y is the distance from the residual surface and y^* is the normalized depth y/h_0.

steeply on going subsurface. To better assess the strains and strain gradients, three vertical lines A-A', B-B' and C-C' are chosen at different locations along the cut surface (identified on the residual surface by green, blue, and magenta dashed lines respectively). The plastic strain into the normalized depth at each of these locations is shown in Fig. 18b.

The greatest strains occur at the free surface: The precise values (respectively 16, 12 and 10 at A-A', B-B' and C-C') are less important than the fact that the curves are almost coincident below a normalized depth of about 0.1 h_0. Evidently, the strain gradients into the depth are very large close to the surface and become more gradual subsequently: The strains fall from a value bigger than 10 to about 2 within a depth of just 0.25 h_0; $\bar{\varepsilon}$ is about 1 at a depth of 0.50 h_0. The strains fall to a negligibly small value of about 0.3 at a depth of h_0. These high, near-surface strain gradients are also consistent with the highly-sheared and differentially deformed residual surface grains in this simulation (Fig. 7b).

While high fidelity experimental data from type-I chip formation corresponding to the strain data shown in Fig. 18b is currently unavailable, our observations are consistent with the formation of a highly-strained, hardened cut-layer in machining annealed soft metal [14, 49]. In addition, qualitatively similar cut-surface strain fields were observed by Yeung et

27

al. (see Fig. 1 of [41]).

4.3. Remeshing for polycrystalline aggregate cutting

It is interesting to note that while remeshing in homogeneous machining is widely-used [24, 27, 28] to the point of being 'routine', the introduction of microstructure necessitates careful consideration of a number of additional issues while designing remeshing simulations. These include not only the more obvious microstructure-related aspects like grain-splitting and grain-tracking, but also the precise nature of material separation in machining and the kinematics of flow near the tool tip (Sec. 2.3.2).

Indeed, the presence of grains and their deformation prior to splitting makes it evident that it is inaccurate to consider remeshing schemes to simulate metal cutting as 'deformation only / plasticity-and-flow only', as is often assumed [25, 50]. Instead, remeshing without an explicit ductile failure criterion should be considered as a numerical approximation of the process of plastic deformation to the point of rupture, a phenomenon which has been investigated in the past under conditions of high hydrostatic compression [51, 52].

A pure Lagrangian FE analysis with a predefined separation layer can also be used to simulate a limited subset of polycrystalline aggregate cutting processes [22]. However, it is important to compare to what extent their predicted outcomes differ under nearly similar cutting conditions. Two such comparable pairs of simulations are available (The cutting speed V, material models / phases, and h_0 are identical though the grain sizes are slightly different, 100 μm vs 135 μm): Cutting of copper at $\alpha = 0/0.5°$, $\mu = 0.1$ and cutting $\alpha = 45°$, $\mu = 0.1$. The results of these simulations using the two different schemes are compared below:

1. **Suppression of sinuous flow in high rake-angle cutting** For high rake-angle cutting ($\alpha = 45°$), both remeshing (Fig. 11 a,b) and separation (Figs. 6 a,b in [22]) predict similar outcomes in terms of suppression of sinuous flow, chip thickness (1.6 vs 1.7), mid-thickness chip strain (1.58 vs 1.61), deformed grain pattern and so on. Moreover, both sets of results agree very well with the *in situ* experimental observations at $\alpha = 45°$ (Fig. 11c).

However, in remeshing, there is a thin layer of intensely high strain along the face of the chip in contact with the tool. With predefined separation, this layer is not present, and the maximum strain along the rake face is about 2. Clearly, the overall cutting response is not really sensitive to the presence of this layer. Interestingly, a similar phenomenon occurs in indentation of annealed copper by a narrow-angle wedge: boundary conditions that allow easy separation along the symmetry line [53], and those that model the material as deforming to rupture show strain fields that are quite similar except in a thin zone lying along the indenter face [54]. In that instance, the solutions are best considered as providing bounds on all possible indentation responses with a range of ductile failure behaviors. An analogous view can be adopted here : Deformation to rupture is certainly one extreme of ductile material response, while the use of a predefined separation layer represents somewhat easier separation of the material.

The above discussion should be considered with the proviso that remeshing simulations have a finite tip radius while the separation simulations do not; a smaller radius would likely reduce the thickness of such a layer.

2. **Sinuous flow in low friction, low rake-angle cutting** Both schemes predict sinuous flow at low angle $\alpha = 0°/\alpha = 0.5°$ and low-friction $\mu = 0.1$, but the extent of sinuous flow is (surprisingly) higher with a predefined separation layer (Figs. 3,4 in [22]) than when a remeshing criterion is used. The difference is too large to be on account of the difference in grain-size and slight (0.5°) difference in rake-angle. One possible explanation is that in the separation model, all of the material above the separation layer is forced into the chip, thus increasing its volume. Another possible explanation is that the cut length in the remeshing simulation is much smaller than in the simulation with separation, but a comparison of the cutting forces at time $t = 0.2$ s, when the cut-length is 1 mm in both simulations shows that F_x is higher with separation (about 140 N/mm) than with remeshing (about 110 N/m). Similarly, the corresponding chip thickness ratio λ is higher with separation (~ 4) than with remeshing (~ 3.5). More simulations are needed to explain and resolve this difference.

However, it should be noted that both schemes correctly predict that F_x and λ are much higher when sinuous flow does occur, than when it does not (e.g. with $\alpha = 45°$). Note that the higher friction $\mu = 0.3$ and $\mu = 0.5$ simulations cannot be performed without the use of remeshing.

It is also interesting to consider the actual line / curve of material separation in a remeshing framework; such a curve is a boundary between material that flows into the chip and the cut surface, and can be constructed by tracking a Lagrangian grid in the specimen. Fig. 19 shows this curve of material separation for the $\mu = 0.3$, $\alpha = 0.5°$ analysis (dotted line); a horizontal separation line (solid line) is superimposed for comparison. The undeformed microstructure is shown in the background.
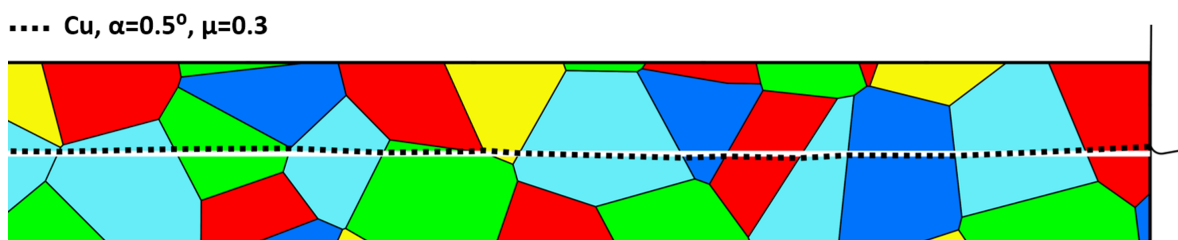

Figure 19: Actual curve of material separation in the $\mu = 0.3$, $\alpha = 0.5°$ analysis (dotted line) compared with horizontal separation (solid line). The background shows the undeformed microstructure.

While deviations from the horizontal occur in both directions, with a maximum value of $7\,\mu$m, the horizontal is very close to the mean of the physical separation curve. The maximum deviation is slightly smaller for the $\alpha = 45°$ analysis, at about $5\,\mu$m. The deviation of the curve is expected to be higher as the extent of sinuous flow increases, e.g. at much higher values of μ.

Lastly, cutting with remeshing, while physically more accurate, is computationally intensive. Table 3 shows representative computational times for a single analysis and remeshing step on a standard desktop computer. Each such step takes 50-75 minutes, of which about one-third is spent in remeshing, tracking, and mapping of field variables. In contrast, it takes only about 8 minutes to cut the same length using a predefined separation layer.

Table 3: Typical wallclock times for single analysis and remeshing steps in polycrystalline Cu cutting

Simulation	Analysis time in solver	Time in custom code and Gmsh	Corresponding cut distance
$\alpha = 0.5°$, $\mu = 0.5$	40 min	20 min	25-50 μm
$\alpha = 0.5°$, $\mu = 0.3$	40-60 min	15 min	25-50 μm
$\alpha = 45°$, $\mu = 0.1$	40 min	10 min	25-50 μm

4.4. Sensitivity of results in remeshing scheme and potential extensibility

The remeshing / mapping scheme is quite complex, with a number of possible modeling choices ranging from grain splitting criteria to constitutive models for the microstructure. The extent to which these choices affect the results demands consideration.

The grain splitting criterion used in this work (Sec. 2.3.2) is physically reasonable, being based on *in situ* imaging experiments (e.g. Fig. 16). Of course, it is possible to devise alternative splitting criteria. Sinuous flow itself is unlikely to be greatly affected by choosing such an alternative, since it is a surface-dominated phenomenon. However, residual surface strains are very sensitive to near-tip conditions, including the tool-tip radius. The inclusion of an explicit ductile failure criterion, which would be required for less ductile materials, would also alter the residual surface strains.

Similarly, the microstructure is modeled using a pseudograin model in the present work: This is a phenomenological model that ignores elastic anisotropy and idealizes grain boundaries as perfect, among other approximations. However, there is nothing that precludes the use of more complex models like direct CPFE [55] with dislocation-physics based plasticity, grain sliding, grain substructure formation etc in the present remeshing framework. Indeed, the extent of sinuous flow is expected to be enhanced by the addition of features like grain boundary sliding. Note that the advantage conferred by direct CPFE over phenomenological models diminishes at large strains ($\bar{\varepsilon} > 1$) due to the extremely complex physics governing microstructural and crystallographic evolution [56].

Lastly, it is possible to extend the present scheme to conduct coupled thermal-stress analyses for cutting at high speeds, or to analyze materials with lower thermal diffusivity.

Conclusions

A new, general remeshing and mesh-to-mesh transfer scheme was presented to simulate the cutting of soft polycrystalline aggregates using a pseudograin model. Importantly, there is no need for a predefined separation layer, and there are no restrictions on the friction, rake angle, or grain-size. The simulations successfully reproduce many experimentally observed aspects of cutting soft, 'gummy' metals, including sinuous flow, surface fold formation, and thick mushroom-like type-I chips at low rake-angle as well as thin, type-II chips with shear-plane like instantaneous deformation fields at high rake-angle. Importantly, the method allows accurate analysis of the cut surface, capturing the high strains, strain gradients and deformed grain shapes in the wake of the tool. The present method is a numerical approximation to model deformation to the point of rupture in highly ductile polycrystalline metal. The method has several advantages over the the traditional 'separation line' technique.

Acknowledgments

References

[1] J. S. Strenkowski, J. T. Carroll, A finite element model of orthogonal metal cutting, J. Eng. Ind. 107 (4) (1985) 349–354.

[2] T. Tyan, W. H. Yang, Analysis of orthogonal metal cutting processes, Int. J. Numer. Meth. Eng. 34 (1) (1992) 365–389.

[3] A. J. Shih, Finite element simulation of orthogonal metal cutting, J. Eng. Ind. 117 (1) (1995) 84–93.

[4] E. Ceretti, P. Fallböhmer, W. T. Wu, T. Altan, Application of 2D FEM to chip formation in orthogonal cutting, J Mater. Process. Tech. 59 (1-2) (1996) 169–180.

[5] R. T. Coelho, E.-G. Ng, M. A. Elbestawi, Tool wear when turning hardened AISI 4340 with coated PCBN tools using finishing cutting conditions, Int J. Mach. Tool Manu. 47 (2) (2007) 263–272.

[6] Y. Zhang, J. C. Outeiro, T. Mabrouki, On the selection of Johnson-Cook constitutive model parameters for Ti-6Al-4 V using three types of numerical models of orthogonal cutting, Procedia CIRP 31 (2015) 112–117.

[7] P. J. Arrazola, T. Özel, Investigations on the effects of friction modeling in finite element simulation of machining, Int. J. Mech. Sci. 52 (1) (2010) 31–42.

[8] J. M. Rodriguez Prieto, J. M. Carbonell, P. Jonsén, Numerical methods for the modelling of chip formation, Arch. Comput. Method. E. (2018).

[9] M. M. Gurusamy, B. C. Rao, On the performance of modified Zerilli-Armstrong constitutive model in simulating the metal-cutting process, Journal of Manufacturing Processes 28 (2017) 253–265.

[10] S. N. Melkote, W. Grzesik, J. Outeiro, J. Rech, V. Schulze, H. Attia, P.-J. Arrazola, R. M'Saoubi, C. Saldana, Advances in material and friction data for modelling of metal machining, CIRP Ann. - Manuf. Techn. (2017).

[11] A. Udupa, K. Viswanathan, Y. Ho, S. Chandrasekar, The cutting of metals via plastic buckling, Proc. R. Soc. A 473 (2202) (2017) 20160863.

[12] K. Viswanathan, A. Udupa, H. Yeung, D. Sagapuram, J. B. Mann, M. Saei, S. Chandrasekar, On the stability of plastic flow in cutting of metals, CIRP Ann. - Manuf. Techn. 66 (1) (2017) 69–72.

[13] H. Yeung, K. Viswanathan, A. Udupa, A. Mahato, S. Chandrasekar, Sinuous flow in cutting of metals, Phys. Rev. Appl. 8 (5) (2017) 054044.

[14] K. Nakayama, The formation of saw-toothed chip in metal cutting, in: Proceedings of the International Conference on Production Engineering, Tokyo, Vol. 1, 1974, pp. 572–577.

[15] E. Usui, A. Gujral, M. C. Shaw, An experimental study of the action of CCl_4 in cutting and other processes involving plastic flow, Int. J. Mach. Tool D. R. 1 (3) (1961) 187–197.

[16] N. K. Sundaram, A. Mahato, Y. Guo, K. Viswanathan, S. Chandrasekar, Folding in metal polycrystals: Microstructural origins and mechanics, Acta Mater. 140C (2017) 67–78.

[17] L. Chuzhoy, R. DeVor, S. Kapoor, A. Beaudoin, D. Bammann, Machining simulation of ductile iron and its constituents, Part 1: Estimation of material model parameters and their validation, J. Manuf. Sci. E. 125 (2) (2003) 181–191.

[18] L. Chuzhoy, R. DeVor, S. Kapoor, Machining simulation of ductile iron and its constituents, Part 2: Numerical simulation and experimental validation of machining, J. Manuf. Sci. E. 125 (2) (2003) 192–201.

[19] A. Simoneau, E. Ng, M. A. Elbestawi, Surface defects during microcutting, Int. J. Mach. Tool Manu. 46 (12-13) (2006) 1378–1387.

[20] T. Mabrouki, C. Courbon, D. Fabre, I. Arrieta, P.-J. Arrazola, J. Rech, Influence of microstructure on chip formation when broaching ferritic-pearlitic steels, Procedia CIRP 58 (2017) 43–48.

[21] Z. Wang, J. Zhang, Z. Xu, J. Zhang, H. ul Hassan, G. Li, H. Zhang, A. Hartmaier, F. Fang, Y. Yan, et al., Crystal plasticity finite element modeling and simulation of diamond cutting of polycrystalline copper, Journal of Manufacturing Processes 38 (2019) 187–195.

[22] A. S. Vandana, N. K. Sundaram, Simulation of sinuous flow in metal cutting, Trib. Lett. 66 (3) (2018) 94.

[23] L. Zhang, On the separation criteria in the simulation of orthogonal metal cutting using the finite element method, J. Mater. Process. Tech. 89 (1999) 273–278.

[24] V. Madhavan, S. Chandrasekar, T. Farris, Machining as a wedge indentation, J. Appl. Mech. 67 (1) (2000) 128–139.

[25] P. Rosa, P. Martins, A. Atkins, Revisiting the fundamentals of metal cutting by means of finite elements and ductile fracture mechanics, Int. J. Mach. Tool Manu. 47 (3) (2007) 607–617.

[26] G. S. Sekhon, J. L. Chenot, Numerical simulation of continuous chip formation during non-steady orthogonal cutting, Eng. Computation. 10 (1) (1993) 31–48.

[27] K. C. Ee, O. W. Dillon Jr, I. S. Jawahir, Finite element modeling of residual stresses in machining induced by cutting using a tool with finite edge radius, Int. J. Mech. Sci. 47 (10) (2005) 1611–1628.

[28] K. Liu, S. N. Melkote, Finite element analysis of the influence of tool edge radius on size effect in orthogonal micro-cutting process, Int. J. Mech. Sci. 49 (5) (2007) 650–660.

[29] A. Svoboda, D. Wedberg, L.-E. Lindgren, Simulation of metal cutting using a physically based plasticity model, Model. Simul. Mater. Sc. 18 (7) (2010) 075005.

[30] M. F. Ashby, The deformation of plastically non-homogeneous materials, Philos. Mag. 21 (170) (1970) 399–424.

[31] S. V. Harren, R. J. Asaro, Nonuniform deformations in polycrystals and aspects of the validity of the taylor model, J. Mech. Phys. Solids 37 (2) (1989) 191–232.

[32] I. Benedetti, F. Barbe, Modelling polycrystalline materials: an overview of three-dimensional grain-scale mechanical models, Journal of Multiscale Modelling 5 (01) (2013) 1350002.

[33] J.-F. Remacle, J. Lambrechts, B. Seny, E. Marchandise, A. Johnen, C. Geuzainet, Blossom-quad: A non-uniform quadrilateral mesh generator using a minimum-cost perfect-matching algorithm, Int. J. Numer. Meth. Eng. 89 (9) (2012) 1102–1119.

[34] J.-F. Remacle, F. Henrotte, T. Carrier-Baudouin, E. Béchet, E. Marchandise, C. Geuzaine, T. Mouton, A frontal delaunay quad mesh generator using the l$^\infty$ norm, Int. J. Numer. Meth. Eng. 94 (5) (2013) 494–512.

[35] N.-S. Lee, K.-J. Bathe, Error indicators and adaptive remeshing in large deformation finite element analysis, Finite Elem. Anal. Des. 16 (2) (1994) 99–139.

[36] S. Léger, A. Fortin, C. Tibirna, M. Fortin, An updated Lagrangian method with error estimation and

adaptive remeshing for very large deformation elasticity problems, Int. J. Numer. Meth. Eng. 100 (13) (2014) 1006–1030.

[37] G. R. Johnson, W. H. Cook, A constitutive model and data for metals subjected to large strains, high strain rates and high temperatures, in: Proceedings of the 7th International Symposium on Ballistics, Vol. 21, The Netherlands, 1983, pp. 541–547.

[38] S. J. Vachhani, S. R. Kalidindi, Grain-scale measurement of slip resistances in aluminum polycrystals using spherical nanoindentation, Acta Mater. 90 (2015) 27–36.

[39] T. Marusich, M. Ortiz, Modelling and simulation of high-speed machining, Int. J. Numer. Meth. Eng. 38 (21) (1995) 3675–3694.

[40] G. T. Camacho, M. Ortiz, Adaptive Lagrangian modelling of ballistic penetration of metallic targets, Comput. Method. Appl. M. 142 (3-4) (1997) 269–301.

[41] H. Yeung, K. Viswanathan, W. D. Compton, S. Chandrasekar, Sinuous flow in metals, Proc. Nat. Acad. Sci. 112 (32) (2015) 9828–9832.

[42] S. Ramalingam, E. Doyle, D. Turley, On chip curl in orthogonal machining, J. Eng. Ind. 102 (1980) 177.

[43] Y. Guo, C. Saldana, W. D. Compton, S. Chandrasekar, Controlling deformation and microstructure on machined surfaces, Acta Mat. 59 (11) (2011) 4538–4547.

[44] B. Ackroyd, S. Chandrasekar, W. D. Compton, A model for the contact conditions at the chip-tool interface in machining, J. Tribol. - T. ASME 125 (3) (2003) 649–660.

[45] S. Lee, J. Hwang, M. R. Shankar, S. Chandrasekar, W. D. Compton, Large strain deformation field in machining, Metall. Mater. Trans. A 37 (5) (2006) 1633–1643.

[46] J. A. Bailey, S. Jeelani, Determination of subsurface plastic strain in machining using an embossed grid, Wear 36 (2) (1976) 199–206.

[47] S. Jeelani, K. Ramakrishnan, Subsurface plastic deformation in machining annealed 18% ni maraging steel, Wear 81 (2) (1982) 263–273.

[48] Y. Guo, R. M'Saoubi, S. Chandrasekar, Control of deformation levels on machined surfaces, CIRP Ann. - Manuf. Techn. 60 (1) (2011) 137–140.

[49] Y. Guo, C. Saldana, J. B. Mann, R. M'Saoubi, S. Chandrasekar, Deformation and microstructure in machining, Adv. Mat. Res. 223 (2011) 325–331.

[50] A. Atkins, Modelling metal cutting using modern ductile fracture mechanics: Quantitative explanations for some longstanding problems, Int. J. Mech. Sci. 45 (2) (2003) 373–396.

[51] H. L. D. Pugh, D. Green, The effect of hydrostatic pressure on the plastic flow and fracture of metals, Proceedings of the Institution of Mechanical Engineers 179 (1) (1964) 415–437.

[52] I. E. French, P. F. Weinrich, The influence of hydrostatic pressure on the tensile deformation and

fracture of copper, Metall. Trans. A 6 (4) (1975) 785.

[53] N. K. Sundaram, Y. Guo, S. Chandrasekar, Modes of deformation and weak boundary conditions in wedge indentation, MRS Communications 2 (2012) 47–50.

[54] N. K. Sundaram, Mechanics of plastic flow past a narrow-angle wedge indenter, Philos. Mag. (2019) 1–21.

[55] F. Roters, P. Eisenlohr, L. Hantcherli, D. D. Tjahjanto, T. R. Bieler, D. Raabe, Overview of constitutive laws, kinematics, homogenization and multiscale methods in crystal plasticity finite-element modeling: Theory, experiments, applications, Acta Mater. 58 (4) (2010) 1152–1211.

[56] D. A. Hughes, N. Hansen, High angle boundaries formed by grain subdivision mechanisms, Acta Materialia 45 (9) (1997) 3871–3886.